MODELING COUPLED REACTIVE FLOW PROCESSES IN FRACTURED CRYSTALLINE ROCK

Emily R. Stein, Jennifer M. Frederick, Glenn E. Hammond, Kristopher L. Kuhlman, Paul E. Mariner, S. David Sevougian

Sandia National Laboratories: P.O. Box 5800, Albuquerque, NM, 87185, ergiamb@sandia.gov

Numerical simulation of a repository for heat-generating nuclear waste in fractured crystalline rock requires a method for simulating coupled heat and fluid flow and reactive radionuclide transport in both porous media (bentonite buffer, surface sediments) and fractured rock (the repository host rock). Discrete fracture networks (DFNs), networks of two-dimensional planes distributed in a three-dimensional domain, are commonly used to simulate isothermal fluid flow and particle transport in fractures, but unless coupled to a continuum, are incapable of simulating heat conduction through the rock matrix, and therefore incapable of capturing the effects of thermally driven fluid fluxes or of coupling chemical processes to thermal processes. We present a method for mapping a stochastically generated DFN to a porous medium domain that allows representation of porous and fractured media in the same domain, captures the behavior of radionuclide transport in fractured rock, and allows simulation of coupled heat and fluid flow including heat conduction through the matrix of the fractured rock.

We apply the method within Sandia's Geologic Disposal Safety Assessment (GDSA) framework to conduct a post-closure performance assessment (PA) of a generic repository for commercial spent nuclear fuel in crystalline rock. The three-dimensional, kilometer-scale model domain contains approximately 4.5 million grid cells; grid refinement captures the detail of 3,360 individual waste packages in 42 disposal drifts. Coupled heat and fluid flow and reactive transport are solved numerically with PFLOTRAN, a massively parallel multiphase flow and reactive transport code.

Simulations of multiple fracture realizations were run to 1 million years, and indicate that, because of the channeled nature of fracture flow, thermally-driven fluid fluxes associated with peak repository temperatures may be a primary means of radionuclide transport out of the saturated repository. The channeled nature of fracture flow gives rise to unique challenges in uncertainty and sensitivity quantification, as radionuclide concentrations at any given location outside the repository depend heavily on the distribution of fractures in the domain.

I. INTRODUCTION

Numerical simulation of a repository for heat-generating nuclear waste in fractured crystalline rock requires a method for simulating coupled heat and fluid flow and reactive radionuclide transport in both porous media (bentonite buffer, surface sediments) and fractured rock (the repository host rock). DFNs are commonly used to simulate isothermal fluid flow and particle transport in fractures, but unless coupled to a continuum, are incapable of simulating heat conduction through the rock matrix. We present a method for mapping a stochastically generated DFN to a porous medium domain that allows representation of porous and fractured media in the same domain, captures the behavior of radionuclide transport in fractured rock, and allows simulation of coupled heat and fluid flow including heat conduction through the matrix of the fractured rock. We apply the method within Sandia's GDSA framework to conduct a post-closure PA of a generic repository for commercial spent nuclear fuel (CSNF) in crystalline rock.

II. EQUIVALENT CONTINUOUS POROUS MEDIUM

Integration of DFNs into the GDSA framework is a collaborative effort between Sandia National Laboratories and Los Alamos National Laboratory (LANL). A DFN is generated with LANL's DFNWorks[1,2] and mapped to an equivalent continuous porous medium (ECPM) with a Python script called mapDFN.

DFNWorks takes as input statistical distributions describing fracture orientation and fracture radii, fracture density (fractures per km^3), parameters relating fracture transmissivity (m^2/s) to fracture radius, and the dimensions of the three-dimensional model domain. It distributes fractures randomly within the space of the model domain and keeps only those fractures that belong to a cluster connecting at least two faces of the domain. For each fracture in a connected cluster, it returns the coordinates of the fracture center, the unit vector defining the pole normal to the plane of the fracture, and the fracture radius, permeability, and aperture (which is calculated as a

function of the fracture transmissivity according to the cubic law[3]).

mapDFN takes as input the output from DFNWorks and parameters describing the desired ECPM model domain and discretization, including the origin and extent of the domain and the size (length) of the cubic grid cells. It determines intersections of fractures with grid cells, and calculates grid cell permeability and porosity from fracture permeability and aperture.

Anisotropic grid cell permeability is calculated by summing the contributions of all the fractures intersecting the cell. For each fracture, intrinsic transmissivity (T_f in m^3) is calculated from permeability (k_f) and aperture (b_f) as

$$T_f = k_f b_f \qquad (1)$$

and described as a tensor, whose coordinates are then rotated into the coordinates of the grid. The resulting tensor, with diagonal and off-diagonal terms, is a complete description of the transmissivity ellipse of the fracture in the coordinates of the ECPM grid. The off-diagonal terms are neglected, and the diagonal tensor describing cell permeability is calculated as

$$\begin{bmatrix} k_{xx} & & \\ & k_{yy} & \\ & & k_{zz} \end{bmatrix} = \frac{1}{d} \sum \begin{bmatrix} T_{xx} & & \\ & T_{yy} & \\ & & T_{zz} \end{bmatrix}_f \qquad (2)$$

where d is the length of the cell side, and the sum is over all fractures intersecting the cell.

In the calculation of porosity, the simplifying assumption is made that each fracture intersecting the cell does so parallel to a face of the cell. Then the porosity (ϕ) of the cell is

$$\phi = \frac{1}{d} \sum b_f, \qquad (3)$$

where d is the length of the cell side, and b_f is the aperture of fracture f. This value is the fracture porosity, which is a very small fraction of the total porosity in a fractured crystalline rock. Applying it to all cells intersected by fractures is critical to simulation of transient transport in the fracture network.

mapDFN assigns all cells in the domain not intersected by fractures user-specified values for matrix (i.e., background) permeability and porosity.

Below, a comparison of results obtained using ECPM and DFN representations of identical fracture networks is presented, followed by a PA of a generic crystalline repository for CSNF performed using ECPM representations of stochastically generated fracture networks.

III. FRACTURE NETWORK STATISTICS

Both the comparison of DFN and ECPM methods and the generic repository PA use stochastically-generated fracture networks, whose statistical definition is based on the well-characterized, sparsely-fractured metagranite at Forsmark, Sweden[4,5]. Fracture networks are comprised of 3 fracture sets (Table 1), each of which is described using a 3-dimensional Fisher distribution for the orientation of fracture poles in space, a truncated power-law distribution for fracture radii, and a fracture density. Fracture density was increased relative to that observed at Forsmark to create percolating fracture networks. Fracture transmissivity is calculated as a function of fracture radius according to[4]

$$\log(T_f) = \log(ar^b), \qquad (4)$$

where T_f is fracture transmissivity (m^2/s), r is fracture radius (m) and a and b are constants with values of 1.6×10^{-9} and 0.8, respectively.

Table 1. DFN parameters (modified from Wang et al.[6]).

Set	Orientation: Fisher Distribution			Radius: Truncated Power Law			Density
	Mean trend	Mean Plunge	κ	α	r_0 (m)	r_x (m)	(km^{-3})
NS	90°	0°	22	2.5	15	500	2,100
EW	180°	0°	22	2.7	15	500	2,000
HZ	360°	90°	10	2.4	15	500	2,300

IV. COMPARISON OF DFN AND ECPM

Simulations of advective transport in DFN and ECPM representations of 10 fracture networks were run using PFLOTRAN[7] and compared by visual inspection, and on the basis of bulk permeability of the model domain and normalized cumulative tracer breakthrough. Fracture networks were generated in cubic model domains 990 m on a side. ECPM domains are discretized into 15 m cubes. To compare directly with the DFN, cells in the ECPM not intersected by a fracture are made inactive. DFN domains averaged 1.6 million grid cells, while ECPM domains averaged 32,000 active grid cells.

North, south, top and bottom boundaries are no flow boundaries. At the west and east boundaries, pressure is held such that a 1 Pa/m pressure gradient drives flow from west to east. Transport simulations use the steady-state flow field. Initial concentrations of tracer are 10^{-8} M throughout the domain, and an initial tracer pulse of 1 M concentration is introduced at the west boundary. The tracer concentration does not affect the steady-state flow simulation.

ECPM simulations ran in a fraction of the time required for DFN simulations (~5 and ~30 minutes to run to 100,000 yr, respectively) and simulation results compare well. The distribution of tracer at 1,000 yr in fracture network "small8" (Fig. 1) is similar in the DFN and ECPM representations except at the southwest corner of the domain, where the 15-m discretization of the ECPM representation resulted in a false connection to the west face of the domain. Bulk permeability (calculated from Darcy's Law[8]) in the ECPM model domains is about 70% of that in the DFN domains (Fig. 2). Tracer arrives at the

east face between approximately 50 and 400 yr in the DFN simulations, and between approximately 90 and 800 yr in the ECPM simulations (Fig. 3).
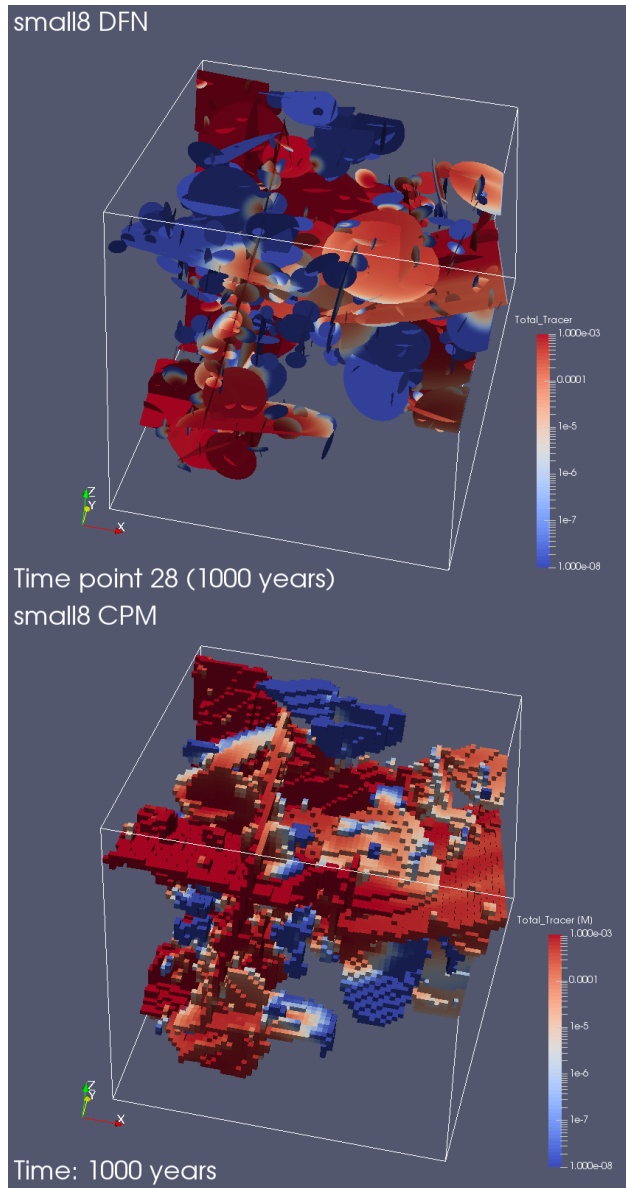

Fig. 1. Distribution of tracer in DFN (top) and ECPM (bottom) representations of fracture network "small8" at 1,000 yr.

False connectivity and increased path length are two known challenges in creating ECPM representations of DFNs[8]. False connections can be minimized with asymmetric representations of permeability[9] without refining the grid discretization. Path lengths (and therefore travel times) are longer in ECPMs because the ECPM converts a sloped fracture plane into a series of stairsteps. Fracture permeability in the ECPM can be corrected to account for the difference in path length[9]. Corrections to

ECPM permeability that minimize false connections and path length discrepancies may be included in the GDSA framework in the future.
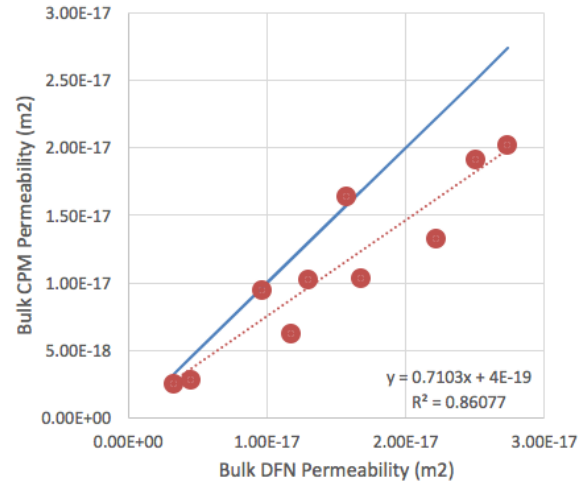

Fig. 2. Bulk permeability of ECPM versus DFN.

V. GENERIC CRYSTALLINE REPOSITORY

The present concept for a mined repository in crystalline rock places the repository approximately half a kilometer below the land surface in a sparsely fractured crystalline rock (such as granite) that either outcrops or subcrops near surface. Regionally, the topographic slope is < 1°, and the water table is unconfined, a combination which would provide little driving force for deep fluid flow. The reference repository site is in a stable cratonic terrain with low probabilities of seismicity, igneous activity, and human intrusion. This concept is consistent with international concepts of disposal in crystalline rock[10].

Locations fitting this concept occur in the eastern half of the United States[11], where outcropping/subcropping crystalline basement is Precambrian to Archean in age[12] and measured heat flow is generally between 35 and 65 mW/m^2 (Ref. 13). At repository depth, the host rock is saturated, with brackish, reducing water[14]. The driving force for regional flow at depth is assumed to be similar to that in deep sedimentary basins, on the order of 10 Pa/m (e.g., Ref. 15).

V.A. Engineered Barriers

It is assumed that a commercial repository would hold 70,000 MTHM of CSNF, which is the maximum allowed by the Nuclear Waste Policy Act of 1983 and about half of the total CSNF inventory predicted by 2055 in the "no replacement scenario"[16]. This inventory could be accommodated in 168 disposal drifts, each 805 m in length, with drift centers separated by 20 m, and waste packages emplaced lengthwise within the drifts with a spacing of 10 m center-to-center[6]. Repository access would be via

vertical shafts and/or a ramp. Approximately one quarter of the 70,000 MTHM inventory is included in 42 disposal drifts in PA simulations.
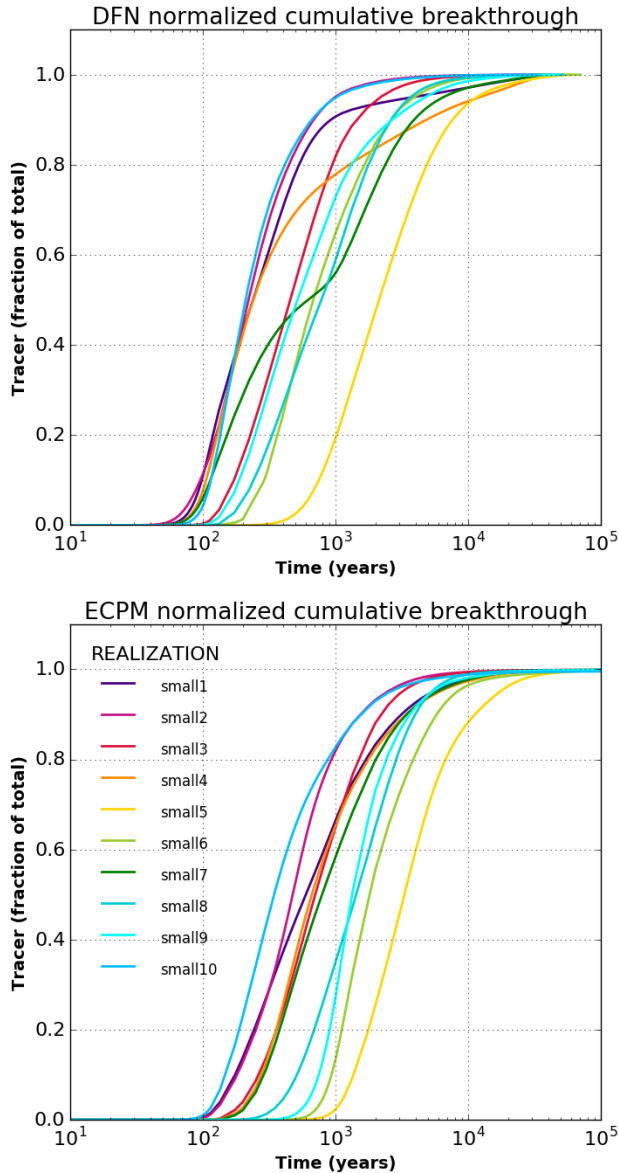
DFN normalized cumulative breakthrough

ECPM normalized cumulative breakthrough

Fig. 3. Normalized cumulative breakthrough in ten DFN (top) and ECPM (bottom) simulations.

V.A.1. Inventory

For simplicity, PA simulations assume the inventory consists entirely of pressurized water reactor (PWR) CSNF assemblies, each containing 0.435 MTHM. Radionuclide inventories and decay heat as a function of time assume an initial enrichment of 4.73 weight-% ^{235}U, 60 GWd/MTHM burn-up, and 100-yr out of the reactor (OoR) storage prior to deep geologic disposal[16]. Because the average burn-up of CSNF under the "no replacement scenario" is predicted

to be only 54 GWd/MTHM (Ref. 16), the assumption of 60 GWd/MTHM results in a conservatively high heat load.

V.A.2. Waste Form

Spent uranium oxide (UO$_2$) fuel is a polycrystalline ceramic material stable to high temperatures. Cladding protects the fuel from degradation in the reactor, and can continue to protect the fuel from degradation in the repository. In the reactor, fuel undergoes physical changes due to heating, radiation damage, and the build-up of fission products. Lighter elements (fission products) become concentrated in voids and the outer margins of the UO$_2$ matrix.

In PA simulations, the waste form is represented as a radionuclide source term within a waste package region. The waste form releases radionuclides in two fractions: instant-release (upon waste package breach) and slow-release (according to the UO$_2$ matrix dissolution rate). Numerical representation of waste form degradation is described in Section VI and by Frederick et al.[17]

V.A.3. Waste Package

The waste package is assumed to consist of a stainless steel canister containing 12 PWR CSNF assemblies (5.22 MTHM) and a stainless steel overpack, 5 meters in length and 1.29 m in diameter. Due to gridding limitations, the size of simulated waste packages is $1.67 \times 1.67 \times 5$ m^3, and is larger in volume than 12-PWR waste packages are expected to be.

Waste package porosity is set equal to the fraction of void space within a waste package, which is 50% (Ref. 18). Permeability is set several orders of magnitude higher than that of the surrounding materials, so that flow through waste packages is uninhibited. The waste package is given the thermal properties of stainless steel[19].

The granite reference case is the first GDSA PA to take credit for waste package performance via calculation of canister vitality, the numerical implementation of which is described in Section VI and by Frederick et al.[17]

V.A.4. Bentonite Buffer

The crystalline reference case assumes horizontal, in-drift emplacement with waste packages elevated on plinths of compacted bentonite and drifts buffered and filled with compacted bentonite pellets and/or bricks in one or two layers[6]. Access halls may be filled with a mixture of crushed rock and bentonite or another geologic material rich in clay minerals[6,20], but the present simulations assume the halls and drifts are both filled with a compacted bentonite buffer.

Compacted bentonite has low permeability, high sorption capacity, and may be engineered to achieve

desirable thermal properties; for instance, quartz sand or graphite can be added to increase its thermal conductivity[21,22,23]. The current set of simulations employs a single layer buffer with material properties appropriate for a compacted mixture of 70% bentonite and 30% quartz sand. The buffer is assigned a porosity of 0.35 (Ref. 24), a permeability of 10^{-20} m^2 (Ref. 24), and a water-saturated thermal conductivity of 1.5 W/m/K (Ref. 23).

V.B. Natural Barriers

V.B.1. Crystalline Host Rock

The representation of fractured crystalline rock is based primarily on the well-characterized, sparsely fractured metagranite at Forsmark, Sweden[4,5]. The Forsmark site sits in the Fennoscandian Shield and consists of crystalline bedrock (primarily granite with lesser amounts of granodiorite, tonalite, and amphibolite) that formed between 1.89 and 1.85 Ga[10]. Recent glaciation (<1 Ma) has resulted in crystalline basement outcrops and thin (<25 m) Quaternary sedimentary deposits of variable thickness and extent[25]. Similar crystalline basement exists within the United States (e.g., the southern margin of the approximately 2-billion-yr-old Superior Craton in Minnesota and Wisconsin[26]).

Fracture properties are described in Section III. Matrix permeability (10^{-20} m^2) and porosity (0.005) are derived from measurements made in tunnel walls of underground research laboratories (URLs) in crystalline rock at the Grimsel Test Site, Switzerland[27,28], Lac du Bonnet batholith, Canada[29], and the Korean Underground Research Tunnel[30]. Fractures and matrix are assumed to have an effective diffusion coefficient of 10^{-12} m^2/s (Ref. 28) and a thermal conductivity of 2.5 W/m/K (Ref. 31).

V.B.2. Disturbed Rock Zone (DRZ)

The DRZ, the portion of the host rock adjacent to the engineered barrier that experiences durable changes due to excavation of the repository, will have elevated permeability due to changes in stress induced by mining.

In-situ DRZ permeability has been measured in URLs in crystalline rock in Korea[30] and Canada[29]. In the Korean URL, gas permeability was as high as 10^{-17} m^2 at distances up to 2 m from the tunnel wall; beyond that distance it was approximately 10^{-20} m^2 (liquid permeabilities are less than low-pressure gas permeabilities)[30]. In the Lac du Bonnet URL, liquid permeability was between 10^{-16} and 10^{-19} m^2 out to 0.3 to 0.5 m from the tunnel wall, beyond which it was between 10^{-22} and 10^{-20} m^2 (Ref. 29).

PA simulations assume a 1.67 m thick DRZ on all sides of emplacement drifts and access halls. DRZ porosity is assumed to be 0.01, twice that of the undisturbed matrix; the effective diffusion coefficient is assumed to be 10^{-11} m^2,

10 times higher than undisturbed host rock; and DRZ permeability is assumed to be 10^{-16} m^2, the highest value measured in the Lac du Bonnet URL[29].

V.B.3. Sedimentary Overburden

The crystalline reference case assumes a 15-m-thick overburden of glacial sediments with porosity (0.2) and permeability (10^{-15} m^2) appropriate for a silty glacial till[8].

VI. POST-CLOSURE PERFORMANCE ASSESSMENT

This preliminary PA assumes an undisturbed repository. Because the PA does not consider the biosphere, the performance metric is maximum radionuclide concentration rather than dose. Simulations assume (1) a mined repository at 585 m depth in fractured crystalline rock; (2) 15 m of unconsolidated sedimentary overburden; and (3) a saturated domain.

Results of 15 fracture realizations are reported below. Mariner et al.[14] present a suite of 50 probabilistic simulations, and discuss uncertainty and sensitivity related to input parameters other than fracture distribution.

VI.A. Numerical Implementation

VI.A.1. Model Domain

The mesh was created with Cubit[32]. The model domain (Fig. 4) is 3,015 m long (x), 2,025 m wide (y), and 1,260 m tall (z). Most of the domain is discretized into 15 m cubes. The repository and adjacent cells are discretized into cells 1.67 m (5/3 m) on a side. The domain contains 4,848,260 cells; of these, approximately 2.5 million are the smaller cells in and around the repository.

Pressures and temperatures are initialized by applying zero liquid flux and an energy flux of 60 mW/m^2 to the base of the domain, while holding temperature (10 °C) and pressure (approximately atmospheric) constant at the top of the domain, and running to 10^6 yr. Pressure at the top of the domain decreases from west (left) to east (right) with a gradient of -13 Pa/m. Simulations include 18 radionuclides (^{241}Am, ^{243}Am, ^{238}Pu, ^{239}Pu, ^{240}Pu, ^{242}Pu, ^{237}Np, ^{233}U, ^{234}U, ^{236}U, ^{238}U, ^{229}Th, ^{230}Th, ^{226}Ra, ^{135}Cs, ^{129}I, ^{99}Tc, ^{36}Cl); initial concentrations of all radionuclides in all cells are 10^{-22} mol/L.

At all faces, initial pressures and temperatures are held constant. Concentration of each radionuclide in fluid entering the model domain is 10^{-22} mol/L, while fluid exiting the model domain is allowed to advect ambient concentrations (no diffusive flux at boundaries).

Material properties are summarized in Table 2.

Table 2. Material properties.

	Log k m^2	ϕ	τ	$D_e^{(b)}$ m^2/s	λ W/m/K	C_p J/kg/K	ρ_g kg/m^3
WP	-16	0.5	1	5×10^{-10}	16.7	466	5000
Buffer	-20	0.35	0.35	1.2×10^{-10}	1.5	830	2700
DRZ	-16	0.01	1	10^{-11}	2.5	830	2700
Matrix	-20	0.005	0.2	10^{-12}	2.5	830	2700
Frac.	a	a	a	10^{-12}	2.5	830	2700
Sed.	-15	0.2	0.2	4×10^{-11}	1.7	830	2700

^{a} Calculated on a cell by cell basis for each fracture realization.

Fifteen fracture realizations were generated for the crystalline reference case from the parameters in Table 1. Each realization contains a single deterministic deformation zone striking NS with a dip of 30° and a transmissivity of 1.5×10^{-6} m^2/s, and approximately 9,000 stochastically generated connected fractures.
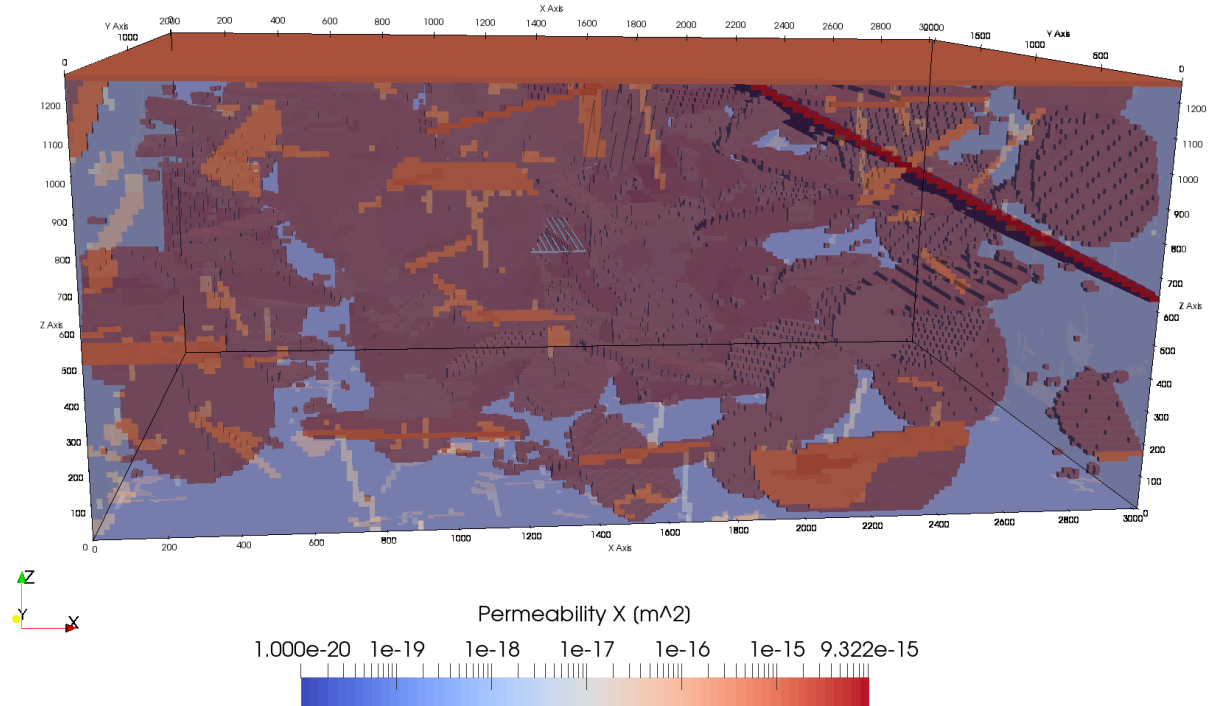
Fig. 4. Model domain colored by permeability. The 3-dimensional structures inside the domain are the repository (colored gray rather than by permeability); the deterministic deformation zone, colored red due to its high permeability; and the largest fractures of a stochastically generated fracture network (Domain6). Permeabilities less than 5×10^{-16} m^2 were not plotted.

VI.A.2. Waste Package Source Terms

Each waste package is modeled as a transient heat source. The energy (watts per waste package) entering the model domain is updated each time step from values in a lookup table. The initial value (3084 W/waste package) is that for PWR CSNF 100 yr OoR. Between times specified in the lookup table, the energy input is linearly interpolated.

The waste package degradation model implemented in PFLOTRAN[13,16] calculates canister vitality at each time step as a function of a base canister degradation rate, a canister material constant, and temperature. Waste package breach occurs when the canister vitality reaches zero. A base canister degradation rate is assigned to each waste package from a truncated log-normal distribution with a mean of $10^{-4.5}$/yr, a standard deviation of 0.5 (log units) and an upper truncation of -3.5 (log units).

PFLOTRAN calculates decay and ingrowth of the radionuclide inventory in each waste package region. From

the time of waste package breach, the waste form releases radionuclides in two fractions: instant-release and slow-release. The instant-release fraction is due to the accumulation of fission products in waste form void spaces and occurs at waste package breach. The crystalline reference case assumes a non-zero instant-release fraction for ^{135}Cs, ^{129}I, ^{99}Tc, and ^{36}Cl (0.1, 0.1, 0.07, and 0.05, respectively[33]), and zero for all other radionuclides. The slow-release fraction is due to fuel matrix (UO$_2$) dissolution, modeled here using a fractional dissolution rate of 10^{-7}/yr starting from the time of waste package breach. This rate is the mode of a log-triangular distribution appropriate for fuel 3,000-10,000 yr OoR under strongly reducing conditions[34].

VI.A.3. Radionuclide Solubility and Sorption

Simulations use element solubility limits calculated by Mariner et al.[19] for a dilute Na-Ca-Cl brine at nearly neutral pH under reducing conditions. I, Cl, and Cs are assumed to

be infinitely soluble. Isotope solubility is calculated assuming that isotope ratios are identical in the solid and aqueous phases[13]. Sorption is modeled using linear distribution coefficients (K_d values)[13]. I and Cl are assumed to be non-sorbing.
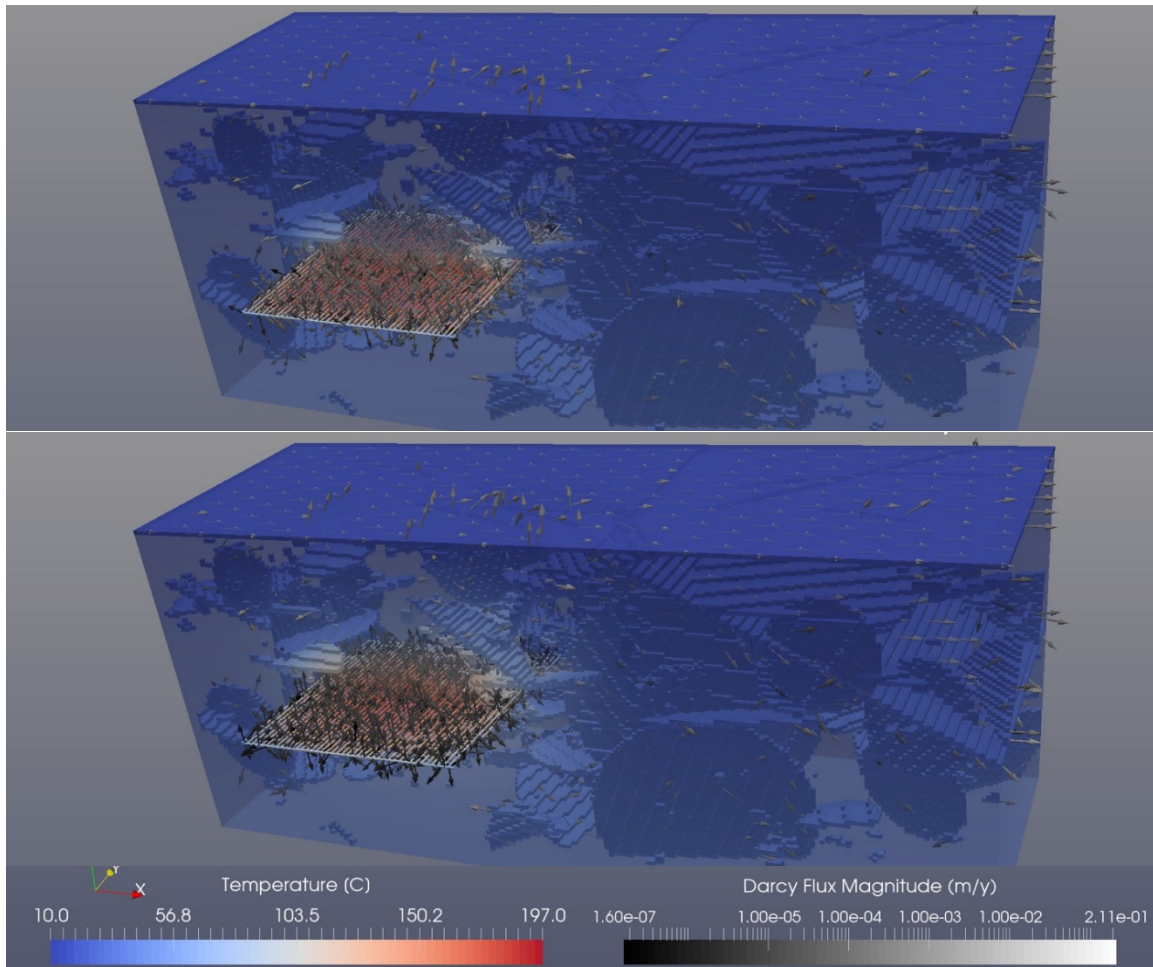

Fig. 5. Temperature field and Darcy flux vectors at 200 yr (top) and 1000 yr (bottom). The entire repository and half of the model domain are plotted. Temperature is 10 ºC at the top of the domain, and ~40 ºC at the base of the domain. Darcy flux in the sediment due to the regional gradient is on the order of 10^{-4} m/yr.

VI.B. Simulation Results

Results are concentrations of the long-lived radionuclides ^{129}I ($t_{1/2}$ = 1.57×10^7 yr) and ^{237}Np ($t_{1/2}$ = 2.14×10^6 yr). ^{129}I is assumed to have unlimited solubility and to be non-sorbing; it thus behaves nearly conservatively. ^{237}Np is solubility-limited and sorbing. Temperature fields, flux vectors, and waste package breach times for a single fracture realization are also presented.

The current PA simulations are limited by their generic nature as well as the bias toward fracture connectivity required to create a percolating network, and should not be interpreted in terms of repository performance in a fractured crystalline host rock. Results can, however, contribute to prioritization of experimental efforts, improve understanding of site-specific data needs, inform optimization of repository design, and lead to improvements in modeling methods and analysis.

Temperature and fluid flow fields at 200 yr and 1,000 yr for the fracture realization "Domain6" are shown in Fig. 5. Temperatures peak just below 200 °C at approximately 200 yr, although maximum fluid fluxes occurred earlier in response to repository warming. The repository remains warmer than background at 1,000 yr, and where fractures intersect the repository, fluid flow out of the repository is still occurring. At 10,000 yr (not shown), repository temperatures are approximately 100 °C. By 100,000 yr repository temperatures have returned to near background, and the repository's thermal influence on the flow field has diminished.

Ten waste packages have breached by 300 y, and ten out of 3,360 waste packages do not breach during the 10^6-yr simulation (Fig. 6). By 400 yr, transport in fractures has carried ^{129}I to the east (right) face of the model domain over 1.5 km from the repository (Fig. 7). At 10^5 yr, diffusion into the host rock matrix is apparent (Fig. 7). At 10^6 yr, ^{237}Np remains within a few meters of the repository (not shown).
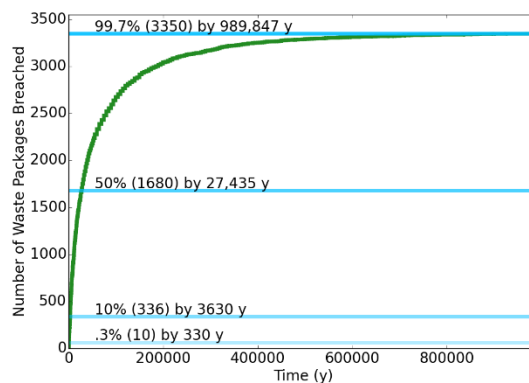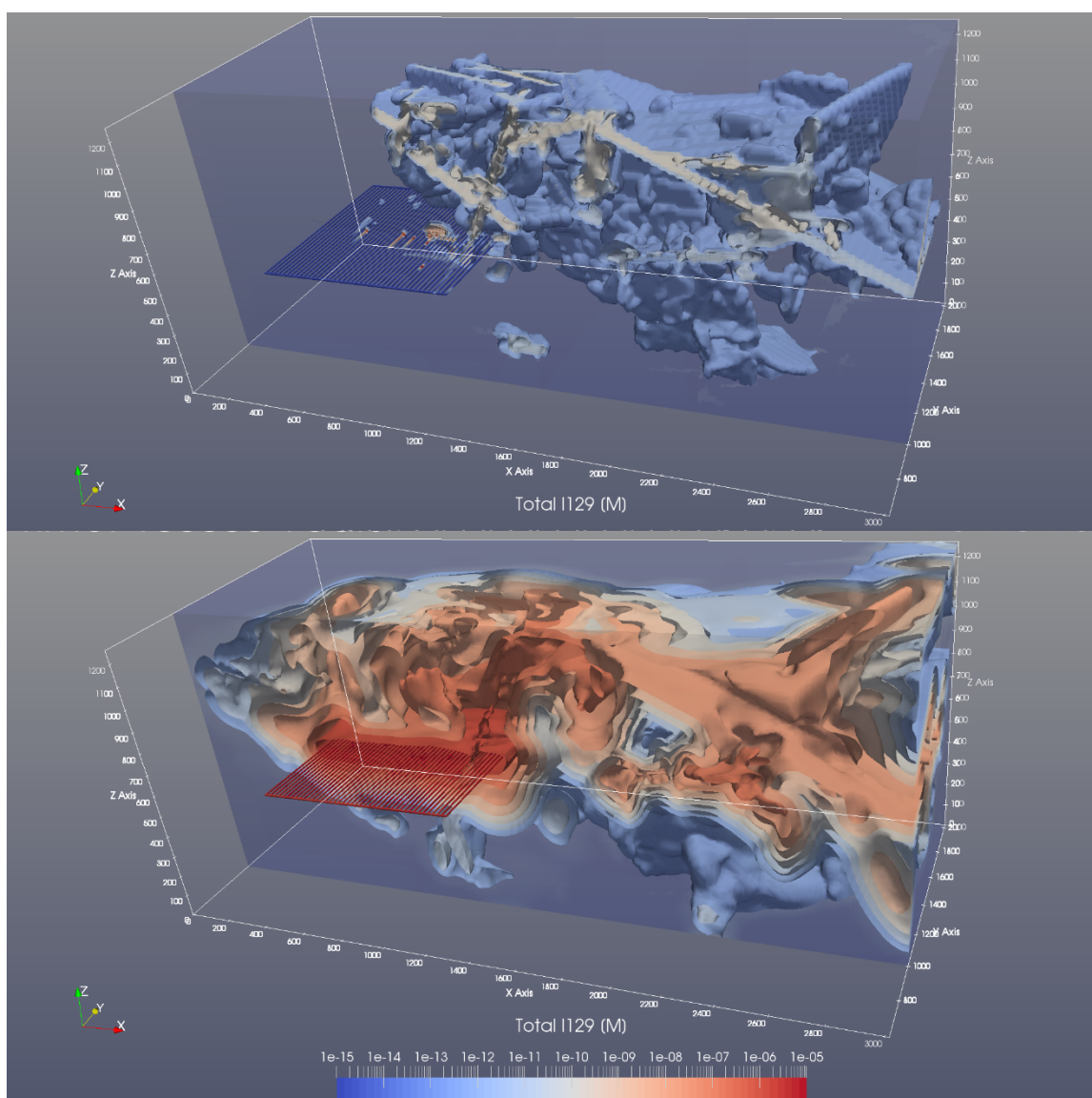

Fig. 6. Cumulative number of waste packages breached.

Fig. 7. ^{129}I concentration at 400 yr (top) and 100,000 yr (bottom).

VI.B.1. Comparing Fracture Domains

Break through curves for [129]I at three observation points in the sediment (Fig. 8) are compared in Fig. 9. Among these sediment observation points, the time of earliest arrival ranges over almost three orders of magnitude, from a few hundred years to approximately 100,000 yr. The observation point with the first [129]I arrival depends on the fracture realization. The two dashed lines indicate two simulations in which [129]I arrived at the furthest point from the repository approximately 300 years into the simulation and at closer observation points thousands to tens of thousands of years later. The maximum concentration of [129]I ranges over approximately four orders of magnitude. The timing of maximum concentration varies between approximately 10^4 and 10^6 years. The time of earliest arrival and the timing and magnitude of maximum concentration at any given point in the domain depend heavily on the connectivity (or lack thereof) between that point and the repository.
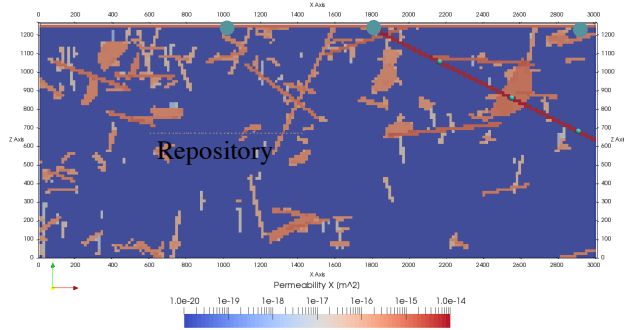

Fig. 8. Observation points (teal circles) are located on the *y* midpoint of the domain. From left to right in uppermost layer (sediments): "glacial1," "glacial2," and "glacial3."

VII. CONCLUSIONS

ECPM representations of fracture networks predict results comparable to those of DFNs. In addition to capturing the behavior of solute transport in fractured rock, ECPMs increase computational efficiency, allow representation of porous and fractured media in the same domain, and are capable of simulating coupled heat and fluid flow including heat conduction through the matrix of the fractured rock.

PA of a generic mined repository in fractured crystalline rock using stochastically generated fracture networks illustrates that plume migration depends on the location of randomly distributed fractures. The uncertainty in magnitude and timing of predicted concentrations at any given location in the model domain is several orders of magnitude. Introduction of a performance metric other than concentration (or dose) at a point location would be useful

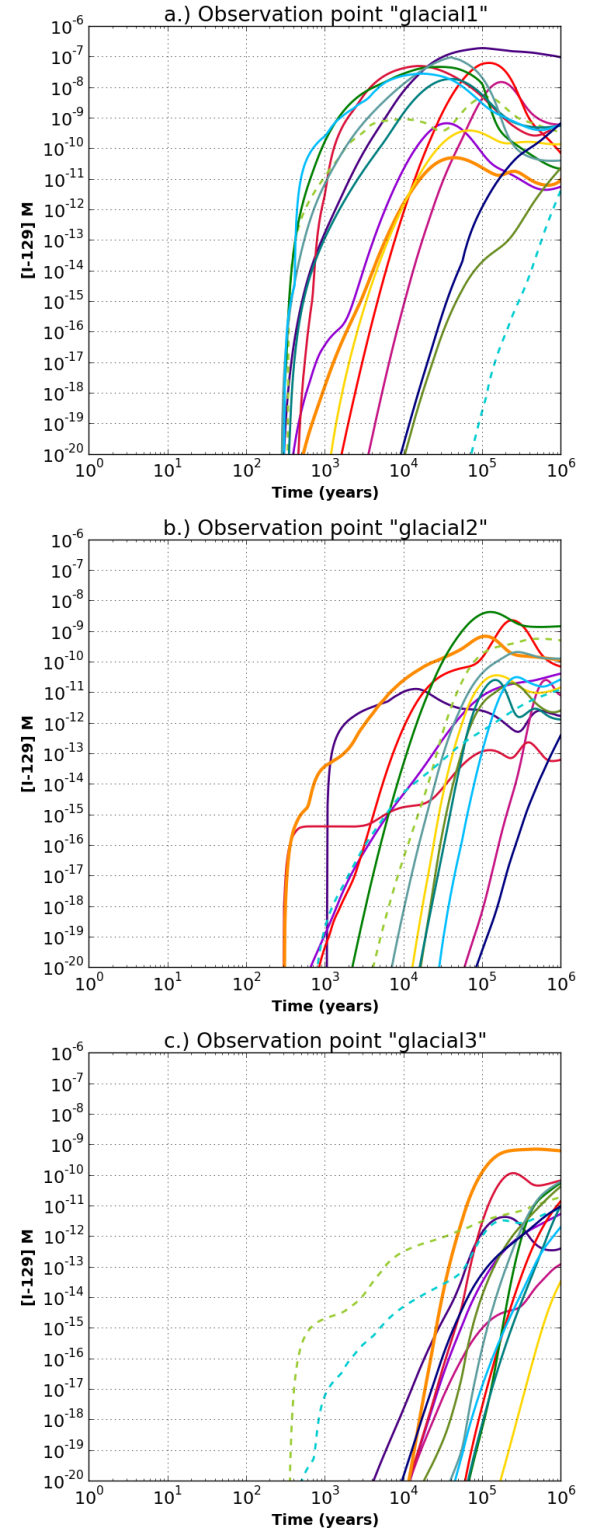in quantifying uncertainty and sensitivity in a fractured system.

Fig. 9. [[129]I] vs. time for 15 fracture realizations at observation points a) glacial1, b) glacial 2, c) glacial3.

The current representation of the fractured host rock is biased toward greater connectivity than is likely to exist in a sparsely fractured rock selected for nuclear waste disposal. Having established the capability of simulating flow and transport in a fractured system, we can in the future 1) determine the influence of deterministic features on flow and transport pathways, and 2) determine the probability of a percolating fracture network existing at various length scales given a realistic description of fractured crystalline rock. If a crystalline rock disposal site is selected, site-specific understanding of deterministic features and of the probability of a percolating network existing at the scales of interest will be necessary.

ACKNOWLEDGMENTS

REFERENCES

1. Hyman, J. D., S. Karra, N. Makedonska, C. W. Gable, S. L. Painter and H. S. Viswanathan (2015). "DFNWorks: A discrete fracture network framework for modeling subsurface flow and transport," *Computers & Geoscience*, **84**:10-19.
2. Hyman, J. D., S. L. Painter, H. Viswanathan, N. Makedonska and S. Karra (2015). "Influence of injection mode on transport properties in kilometer-scale three-dimensional discrete fracture networks," *Water Resources Research*, **51**(9):7289-7308.
3. Bear, J., C. F. Tsang, and G. de Marsily 1993. *Flow and Contaminant Transport in Fractured Rock*. San Diego, CA: Academic Press, Inc.
4. Follin, S., L. Hartley, I. Rhen, P. Jackson, S. Joyce, D. Roberts and B. Swift (2014). "A methodology to constrain the parameters of a hydrogeological discrete fracture network model for sparsely fractured crystalline rock, exemplified by data from the proposed high-level nuclear waste repository site at Forsmark, Sweden," *Hydrogeology Journal*, **22**(2):313-331.
5. Joyce, S., L. Hartley, D. Applegate, J. Hoek and P. Jackson (2014). "Multi-scale groundwater flow modeling during temperate climate conditions for the safety assessment of the proposed high-level nuclear waste repository site at Forsmark, Sweden," *Hydrogeology Journal*, **22**(6):1233-1249.
6. Wang, Y., E. Matteo, J. Rutqvist, J. Davis, L. Zheng, J. Houseworth, J. Birkholzer, T. Dittrich, C. W. Gable, S. Karra, N. Makedonska, S. Chu, D. Harp, S. L. Painter, P. Reimus, F. V. Perry, P. Zhao, J. B. Begg, M. Zavarin, S. J. Tumey, Z. R. Dai, A. B. Kersting, J. Jerden, K. E. Frey, J. M. Copple and W. Ebert (2014). *Used Fuel Disposal in Crystalline Rocks: Status and FY14 Progress*. FCRD-UFD-2014-000060, SAND2014-17992 R. Sandia National Laboratories, Albuquerque, New Mexico.
7. Hammond, G.E., P.C. Lichtner and R.T. Mills (2014) Evaluating the Performance of Parallel Subsurface Simulators: An Illustrative Example with PFLOTRAN, *Water Resources Research*, **50**(1):208-228.
8. Freeze, R. A. and J. A. Cherry (1979). *Groundwater*. Englewood Cliffs, New Jersey, Prentice-Hall, Inc.
9. Parashar, R., and D. M. Reeves (2011). *Computation of flow and transport in fracture networks on a continuum grid*. In: Proceedings of MODFLOW and MORE 2011: Integrated Hydrologic Modeling, Golden, CO. 5–8 June 2011. Int. Ground Water Model. Ctr., Colorado School of Mines, Golden. p. 752–756.
10. SKB (2007). *Geology Forsmark*. R-07-45. Svensk Karnbranslehantering AB, Stockholm, Sweden.
11. Perry, F. V., R. E. Kelley, P. F. Dobson and J. E. Houseworth (2014). *Regional Geology: A GIS Database for Alternative Host Rocks and Potential Siting Guidelines*. LA-UR-14-20368. Los Alamos National Laboratory, Los Alamos, New Mexico.
12. Barton, K. E., D. G. Howell, J. F. Vigil, J. C. Reed and J. O. Wheeler (2003). *The North America Tapestry of Time and Terrain*. Geologic Investigations Series I-2781. United States Geological Survey. Denver, Colorado.
13. Blackwell, D. D., M. C. Richards, Z. S. Frone, J. F. Batir, M. A. Williams, A. A. Ruzo and R. K. Dingwall. (2011). "SMU Geothermal Laboratory Heat Flow Map of the Conterminous United States, 2011," http://www.smu.edu/geothermal. Retrieved August 21, 2015.
14. Mariner, P. E., E. R. Stein, J. M. Frederick, S. D. Sevougian, G. E. Hammond, and D. G. Fascitelli 2016. *Advances in Geologic Disposal System Modeling and Application to Crystalline Rock*. FCRD-UFD-2016-000440. Sandia National Laboratories, Albuquerque, NM.
15. Downey, J. S. and G. A. Dinwiddie (1988). *The Regional Aquifer System Underlying the Northern Great Plains in Parts of Montana, North Dakota, South Dakota, and Wyoming - Summary*. Professional

Paper 1402-A. United States Geological Survey, Washington, DC.

16. Carter, J. T., A. J. Luptak, J. Gastelum, C. Stockman and A. Miller (2013). *Fuel Cycle Potential Waste Inventory for Disposition*. FCRD-USED-2010-000031 Rev 6. Savannah River National Laboratory, Aiken, South Carolina.

17. Frederick, J. M., G. E. Hammond, P. E. Mariner, E. R. Stein and S. D. Sevougian (2017). "Development of a Waste Form Process Model in PFLOTRAN." *Proceedings of the International High Level Radioactive Waste Management Conference, Charlotte, NC, April 9-13, 2017*.

18. Freeze, G., W. P. Gardner, P. Vaughn, S. D. Sevougian, P. Mariner, V. Mousseau and G. Hammond (2013b). *Enhancements to the Generic Disposal System Modeling Capabilities*. SAND2013-10532P. Sandia National Laboratories, Albuquerque, New Mexico.

19. Shelton, S. M. (1934). "Thermal conductivity of some irons and steels over the temperature range 100 to 500 C," *Bureau of Standards Journal of Research*, **12**(4/6):441-450.

20. Mariner, P. E., J. H. Lee, E. L. Hardin, F. D. Hansen, G. A. Freeze, A. S. Lord, B. Goldstein and R. H. Price (2011). *Granite Disposal of U.S. High-Level Radioactive Waste*. SAND2011-6203. Sandia National Laboratories, Albuquerque, New Mexico

21. Choi, H. J. and J. Choi (2008). "Double-layered buffer to enhance the thermal performance in a high-level radioactive waste disposal system," *Nuclear Engineering and Design*, **238**(10):2815-2820.

22. Jobmann, M. and G. Buntebarth (2009). "Influence of graphite and quartz addition on the thermo-physical properties of bentonite for sealing heat-generating radioactive waste," *Applied Clay Science*, **44**(3-4):206-210.

23. Wang, M., Y. F. Chen, S. Zhou, R. Hu, and C. B. Zhou 2015. "A homogenization-based model for the effective thermal conductivity of bentonite-sand-based buffer material". *International Communications in Heat and Mass Transfer*, **68**:43-49.

24. Liu, J. F., Y. Song, F. Skoczylas and J. Liu (2016). "Gas migration through water-saturated bentonite-sand mixtures, CO_x argillite, and their interfaces," *Canadian Geotechnical Journal*, **53**(1):60-71.

25. SKB (2008). *Bedrock hydrogeology Forsmark*. R-08-45. Svensk Karnbranslehantering AB, Stockholm, Sweden.

26. Stone, D., D. C. Kamineni, A. Brown and R. Everitt (1989). "A comparison of fracture styles in 2 granite bodies of the Superior Province," *Canadian Journal of Earth Sciences*, **26**(2):387-403.

27. Schild, M., S. Siegesmund, A. Vollbrecht and M. Mazurek (2001). "Characterization of granite matrix porosity and pore-space geometry by in situ and laboratory methods," *Geophysical Journal International*, **146**(1):111-125.

28. Soler, J. M., J. Landa, V. Havlova, Y. Tachi, T. Ebina, P. Sardini, M. Siitari-Kauppi, J. Eikenberg and A. J. Martin (2015). "Comparative modeling of an in situ diffusion experiment in granite at the Grimsel Test Site," *Journal of Contaminant Hydrology*, **179**:89-101.

29. Martino, J. B. and N. A. Chandler (2004). "Excavation-induced damage studies at the Underground Research Laboratory," *International Journal of Rock Mechanics and Mining Sciences*, **41**(8):1413-1426.

30. Cho, W. J., J. S. Kim, C. Lee and H. J. Choi (2013). "Gas permeability in the excavation damaged zone at KURT," *Engineering Geology*, **164**:222-229.

31. Vosteen, H. D. and R. Schellschmidt (2003). "Influence of temperature on thermal conductivity, thermal capacity and thermal diffusivity for different types of rock," *Physics and Chemistry of the Earth*, **28**(9-11):499-509.

32. Blacker, T., S. J. Owen, M. L. Staten, R. W. Quador, B. Hanks, B. Clark, R. J. Meyers, C. Ernst, K. Merkley, R. Morris, C. McBride, C. Stimpson, M. Plooster and S. Showman (2016). *CUBIT Geometry and Mesh Generation Toolkit 15.2 User Documentation*. SAND2016-1649 R. Sandia National Laboratories, Albuquerque, New Mexico.

33. Sassani, D. C., C. F. Jové Colón, P. Weck, J. L. Jerden, K. E. Frey, T. Cruse, W. L. Ebert, E. C. Buck, R. S. Wittman, F. N. Skomurski, K. J. Cantrell, B. K. McNamara and Z. Soderquist (2012). *Integration of EBS Models with Generic Disposal System Models*. SAND2012-7762P. Sandia National Laboratories, Albuquerque, New Mexico.

34. Sassani, D., J. Jang, P. Mariner, L. Price, R. Rechard, M. Rigali, R. Rogers, E. Stein, W. Walkow and P. Weck (2016). *The On-line Waste Library (OWL): Usage and Inventory Status Report*. FCRD-UFD-2016-000080. Sandia National Laboratories, Albuquerque, New Mexico.